



JAAS

**Radially Resolved Optical Emission Spectral Imaging Study
of an Atmospheric Pressure μ DBD Jet for Elucidating the
Effect of Sample Surface Material on the Underlying
Mechanisms**

Journal:	<i>Journal of Analytical Atomic Spectrometry</i>
Manuscript ID	JA-ART-12-2020-000522.R1
Article Type:	Paper
Date Submitted by the Author:	19-Mar-2021
Complete List of Authors:	Shi, Songyue; Texas Tech University, Department of Chemistry and Biochemistry Finch, Kevin; Texas Tech University, Department of Chemistry and Biochemistry Gamez, Gerardo; Texas Tech University, Department of Chemistry and Biochemistry

SCHOLARONE™
Manuscripts

1
2
3
4
5
6
7
8
9
10

Radially Resolved Optical Emission Spectral Imaging Study of an Atmospheric Pressure μ DBD Jet for Elucidating the Effect of Sample Surface Material on the Underlying Mechanisms

11 Songyue Shi, Kevin Finch, and Gerardo Gamez *

12
13
14
15 Texas Tech University, Department of Chemistry and Biochemistry, Lubbock, TX 79409-41061,

16
17 USA. E-mail: Gerardo.gamez@ttu.edu
18
19
20
21
22
23
24
25
26
27
28
29
30
31
32
33
34
35
36
37
38
39
40
41
42
43
44
45
46
47
48
49
50
51
52
53
54
55
56
57
58
59
60

Abstract

Dielectric barrier discharges are receiving increasing attention as sampling/ionization sources for ambient mass spectrometry. Nevertheless, the underlying mechanisms are not completely understood, particularly when the plasma plume is exposed to a sample surface. Herein, an atmospheric pressure helium micro-dielectric barrier discharge (μ DBD), flowing into open-air and onto a sample surface (floating Cu or LDPE), is studied via optical emission spectroscopy (OES) with radial information extracted through Abel's inversion. Radially resolved optical emission profiles along the axis are shown to shift with respect the line-of-sight counterparts, for some species. The OES images, as well as vibrational and rotational temperature maps, indicate the energy transfers mainly via Penning ionization of N_2 with He metastables to produce N_2^+ , as the plasma plume exits the capillary into open air, while charge transfer with He_2^+ is dominant further downstream, as well as toward the periphery of the plume. In addition, the sample surface is shown to play an important role in the energy transfer mechanisms. For the LDPE sample, the spatial distribution sequence of excited species is similar to the free-flowing counterpart but disappears into the surface, which indicates that excited N_2 further downstream/outer periphery is produced from electron recombination with N_2^+ . On the other hand, the presence of the floating Cu sample results in an intensity peak at the plasma/surface interface for most species. We propose that the temporal evolution of the half-cycle dynamics have a great effect, where the resulting higher electron temperature and density towards the surface of metallic samples favors electron impact excitation. Furthermore, profilometry of the resulting craters in the floating Cu samples revealed a close correlation between their diameter and the width of the N_2^+ emission.

Introduction

Direct solid surface sampling capabilities represent a significant advantage when it comes to chemical analysis¹. For example, all the time and resource consuming sample preparation steps involved in transforming a fraction of a sample into a suitable state for analysis by a technique of interest are avoided, while possibly allowing *in situ* sample analysis to be completed in the field. Furthermore, it may provide access to additional dimensions not typically accessible after sample preparation, such as in the case of depth profiling.

Atmospheric pressure plasma jets (APPJs) have been gaining increased interest for direct solid surface analysis²⁻⁴. For example, plasma-based ambient mass spectrometry sources allow desorption and ionization from solid sample surfaces to give access to molecular and structural information from the analyte of interest in real-time^{5,6}. These sources are typically configured to minimize damage to the sample surface of interest. Recently, an atmospheric pressure dielectric barrier discharge was proposed for the direct solid sampling of metal substrates⁷, where the operating conditions allowed the substrate to be eroded and the removed material was transported to an inductively coupled plasma for mass spectrometry (MS) analysis. Additionally, depth profiling capabilities were demonstrated in that study. Our laboratory is also currently exploring the possibility of implementing a micro dielectric barrier discharge (μ DBD) for direct MS analysis of solid polymer surfaces where the operating conditions are chosen to allow erosion of the substrate for potential depth profiling capabilities.

On the other hand, the underlying mechanisms of such plasma sources are not completely understood. These fundamental processes include the production of relevant plasma reagents and the mechanisms that lead to the analytical signal. In fact, very few plasma diagnostic studies on

1
2
3 APPJs relevant for chemical analysis have examined the influence of the sample surface on such
4
5 fundamental processes, but these works have reported significant changes on some relevant plasma
6
7 species, such as He metastables⁸. Thus, plasma diagnostic studies are needed to gain more
8
9 information into these mechanisms. There are many techniques, with accompanying advantages
10
11 and disadvantages, that can yield critical information regarding the fundamental processes. Optical
12
13 emission spectroscopy (OES) imaging allows obtaining the distribution of excited species in the
14
15 plasma, which can yield valuable insights into the energy distribution pathways⁹⁻¹¹. In addition,
16
17 relevant species give access to calculating fundamental parameters such as the vibrational
18
19 temperature (T_{vib})^{12, 13}, rotational temperature (T_{rot})¹⁴, and excitation temperature (T_{exc})¹⁵ through
20
21 Boltzmann plots, while electron number density (n_e) and electron temperature (T_e) can be obtained
22
23 via Stark broadening¹⁶. OES diagnostics techniques are popular because they are simple, cost-
24
25 effective, and do not perturb the plasma. On the other hand, OES diagnostics have some
26
27 disadvantages including the emission signal being inherently integrated along the line-of-sight
28
29 (LOS), which does not allow to directly measure the emission intensity three-dimensional
30
31 distribution, and local-thermodynamic equilibrium (LTE) has to be assumed for obtaining some
32
33 of the fundamental parameters.

34
35
36
37
38
39
40
41 The main goal of the present study is to obtain further understanding of the underlying
42
43 mechanisms of APPJs relevant for chemical analysis when the plasma effluent is exposed to
44
45 different sample surfaces. For this purpose, radially resolved OES plasma diagnostics of an
46
47 atmospheric pressure μ DBD are realized with a sub-pixel shifting push-broom hyperspectral
48
49 imaging system (SPS-PbHSI)¹⁷. The radially resolved information is extracted with a previously
50
51 developed protocol for Abel's inversion reconstruction based on a Discreet Fourier Transform
52
53 (DFT) algorithm¹⁸. The distribution of excited He I, He₂, N₂, N₂⁺, O I, as well as T_{rot} and T_{vib} maps,
54
55
56
57
58
59
60

1
2
3 as a function of the μ DBD operating conditions are measured in the presence of different sample
4 surfaces. In addition, the maps are correlated to the μ DBD electrical characteristics and the
5 properties of the produced craters. Finally, some insights into the underlying mechanisms are
6 discussed in context with relevant literature.
7
8
9
10
11
12
13
14
15

16 **Experimental**

17 **Pushbroom hyperspectral imaging**

18
19
20 The plasma OES images were acquired with a push-broom hyperspectral imaging system
21 (Pb-HSI)^{19,20}, which allows the collection of hyperspectral datacubes within short acquisition time
22 and high light throughput (Fig. S1). In this system, the emission from the plasma source was
23 collected by a set of triplet lenses and refocused on the entrance slit (H: 13 mm \times W: 10 μ m) of
24 the spectrograph (IsoPlane SCT 320, Princeton Instruments, USA) by another triplet lens. The
25 focusing lens and a 90-degree turning mirror placed in between the lenses were mounted on a
26 linear motorized stage (MTS50-Z8, Thorlabs Ltd., UK). The moving stage allows implementing
27 the push-broom acquisition in the spatial x-dimension by scanning the image horizontally across
28 the spectrograph slit. The 300 grooves/mm grating was used for collecting spectral datacubes at
29 280-409 nm, 394-523 nm, 582-711 nm, and 677-806 nm, where a high-pass glass filter (cut-off
30 wavelength at 500 nm) was added for the last two wavelength windows to minimize the
31 interference from the 2nd order dispersion. The 1800 grooves/mm grating was used to collect at
32 363-381 nm (N_2 second positive system, $C^3\Pi_u - B^3\Pi_g$) and 378-396 nm (N_2^+ first negative system,
33 $B^2\Sigma_u^+ - X^2\Sigma_g^+$).
34
35
36
37
38
39
40
41
42
43
44
45
46
47
48
49
50
51
52
53
54
55
56
57
58
59
60

1
2
3 The spectrograph features an ICCD camera (iStar 334T, Thorlabs Ltd., UK, 1024 x 1024
4 pixels, pixels size of 13 x 13 μm), with no binning, cooled to -20 °C for all the acquisitions. An
5 exposure of 0.1s was used for the 280-409 nm and 394-523 nm windows, while for the other four
6 windows, 15 on-chip accumulations with 0.1s gate duration were applied to compensate for the
7 lower intensities observed. A homemade LabVIEW program allowed the automation of the Pb-
8 HSI acquisition¹⁷ while the hyperspectral information was analyzed and displayed by ImageJ²¹
9 and MATLAB 2018a.

19 **Sub-pixel shifting**

20
21
22
23 The SPS process is a deconvolution method utilized to turn a series of low-resolution
24 images into a high-resolution image by using a higher sampling rate^{22,23}. The implementation and
25 optimization of the SPS to the Pb-HSI was discussed in previous work¹⁷. The acquisition SPS
26 parameters were set as: spectrograph entrance slit width = 10 μm , motor scan step width = 2 μm ,
27 leading to a deconvolution factor of $10/2 = 5$, and the cutoff frequency of the lowpass noise filter
28 was 0.15.

37 **Abel's inversion**

38
39
40 Abel's inversion is a mathematical protocol that allows for converting the convoluted LOS
41 information to the deconvoluted radially resolved distribution when cylindrical symmetry
42 conditions exist²⁴. The optimized DFT-based Abel's inversion reconstruction method
43 implemented here was previously developed for SPS Pb-HSI¹⁸. The reconstruction parameters
44 used in this study were: 3D median noise filter with 3-pixel radius, number of cosine expansions
45 in the Fourier-transform was set to 8, and number of pixels in radial dimension (limited by the
46 image acquisition) set to 100.

Atmospheric pressure dielectric barrier discharge

A μ DBD discussed in previous work was used as the emission source¹⁷. The inter-electrode distance was set to 6 mm. The power-electrode was placed closer to the capillary tip at a distance of 5 mm. The effluent of the plasma made direct contact with the surface of a sample fixed on an independent X-Y-Z stage (Model A, Line Tool Co. USA) with a capillary tip-to-sample distance set to 1 mm. In this study, a low-density polyethylene (LDPE, 0.92 g/cm³, melting point: 110 °C, Boedeker Plastics Inc., USA) block and a copper block (99.9% purity, Multipurpose 110 Copper, McMaster-Carr, USA) were used as model samples. The helium discharge gas (99.999% purity, Ultra High Purity 5.0 Grade Helium, Airgas, USA) flow rate was varied from 0.1 to 0.4 L/min by a mass flow controller (EW-32907-67, Cole-Parmer, USA). The plasma was powered by an alternating current (AC) generator (PVM500, Information Unlimited, USA) with a frequency of 30 kHz, and applied voltage varied from 6 kV to 8 kV.

Electrical characterization

The applied voltage and frequency were measured with an oscilloscope (DSOX3034A-Digital Storage Oscilloscope, Agilent Technologies, USA) through a high-voltage probe (1000:1 attenuation, P6015A High-Voltage Passive Probe, TEKTRONIX, USA). The current was calculated through the measured potential drop over a 1 k Ω resistor (10:1, N2863B Oscilloscope Probe, Agilent Technologies, USA). A nitrogen displacement gas was used instead of the helium plasma gas to achieve a higher breakdown voltage and ensure no plasma was generated during

displacement current measurements²⁵. The nitrogen displacement gas (99.999 % purity, NI 300 UHP, Airgas, USA) was introduced independently into the μ DBD through a stainless-steel T-piece union fitting (SS-400-3, 1/4 inch tube OD., Swagelok, USA) with a flow rate ranged from 0.1-0.4 L/min.

Determination of plasma temperatures

Vibrational temperature

T_{vib} is an important property used in plasma diagnostics. For example, in nitrogen-containing plasmas, i.e. ambient dielectric barrier discharges, the inelastic collision between the free electrons and the nitrogen is very efficient and the T_{vib} very rapidly equilibrates with the T_e ¹³. The Boltzmann plot is a well-established method for the determination of the plasma temperature through the relative line intensities. According to the Boltzmann Law, the number of molecules excited to certain vibrational states is proportional to $e^{-\frac{E_v}{k_B T}}$, where E_v is the vibrational energy, and it has the following relationship with band intensities^{12, 26}:

$$I_{\nu', \nu''} = C \nu^4 A(\nu', \nu'') e^{-\frac{E_v}{k_B T}} \quad (1)$$

$$\text{or} \quad \ln\left(\frac{I_{\nu', \nu''}}{\nu^4 A(\nu', \nu'')}\right) = -\frac{1}{k_B T} E_v + C \quad (2)$$

where C is an experimental constant, ν' is the vibrational quantum number of the upper state, ν'' is the vibrational quantum number of the lower state, $A(\nu', \nu'')$ is the transition probability, and ν is the wavenumber of the band head, k_B is the Boltzmann constant, and T is the temperature. Here in this study, the second positive system of the N_2 transition ($C^3\Pi_u \rightarrow B^3\Pi_g$) is used to determine the T_{vib} of the plasma from the slope of the plot²⁷. Three band heads in the N_2 ($C \rightarrow B$)

1
2
3 transition measured in the 363-381nm window (1800 grating) are used for the Boltzmann plot:
4
5 $N_2(2 \rightarrow 4)$ at 370.9 nm, $N_2(1 \rightarrow 3)$ at 375.4 nm, and $N_2(0 \rightarrow 2)$ at 380.4 nm, respectively. The radially
6
7 resolved emission is subsequently used to calculate the radially resolved T_{vib} . Good linearity is
8
9 shown in the plots with $R^2 > 0.99$.

12 13 ***Rotational temperature***

14
15
16 The T_{rot} is another important fundamental parameter for plasma diagnostics, corresponding
17
18 to the distribution of the molecular rotational states. A rapid equilibrium can be accomplished
19
20 between the molecular rotational states and the translational energies of the molecules; therefore,
21
22 it is commonly agreed that the T_{rot} is very close to the gas kinetic temperature (T_g)^{28, 29}. Here, the
23
24 T_{rot} was determined by fitting simulated spectra to the experimental spectra at selected positions
25
26 in the radially resolved images. The experimental spectra are obtained from the rotational
27
28 transitions of the N_2^+ first negative system ($B^2\Sigma_u^+ \rightarrow X^2\Sigma_g^+$) in 378-396 nm window (1800
29
30 grating). The wavelength range of interest is from 389.67 to 390.55 nm, which includes eight peaks
31
32 of the R branches from $K''=13$ to $K''=6$ of the N_2^+ band³⁰. The simulated spectra are computed
33
34 using LIFBASE 2.1.1³¹ with a total resolution of 0.7664 nm (instrumental response and other
35
36 broadening), pressure of 760 Torr in air, and a Voigt line shape with 15% Lorentzian. Fig. S2
37
38 shows the comparison between the experimental and simulated spectrums and the best-fit T_{rot} was
39
40 determined by the lowest Chi-square value (χ^2) obtained.

41 42 43 **Erosion crater characterization**

44
45
46 The erosion crater shape and depth were measured by a non-contact optical profilometer
47
48 (WYCO NT2000, Veeco, USA) based on a Mirau interference microscope. The phase-shifting
49
50 interferometry mode (PSI) allowed the depth resolution of 0.1 nm with the height range <160 nm.
51
52 The total scan region was 1.236 x 1.236 mm, and the detector is 736 x 736 pixels. The lateral
53
54
55
56
57
58
59
60

1
2
3 spatial resolution is limited by the 1.68 μm pixel size. The data from the measurements were
4
5 displayed and analyzed by the WYCO Vision 32 software and MATLAB 2018a.
6
7
8
9

10 11 **Results**

12 13 14 **Line-of-sight optical emission spectra**

15
16
17 It is instructive to look at the LOS spectral datacubes along the axial dimension to obtain
18 an overview of the excited species. **Fig. 1** shows significantly different intensity distributions for
19 selected spectral windows at the axial position 0.5 mm inside (**Fig. 1a,c,e,g**) or outside (**Fig.**
20 **1b,d,f,h**) of the capillary tip under the same plasma operating conditions. For example, in the 280-
21 409 nm window inside the capillary (**Fig. 1a**) the N_2^+ emission (391 nm) is most intense while the
22 N_2 bands are about an order of magnitude less intense. In contrast, the region outside the capillary
23 (**Fig. 1b**) shows overall higher and comparable intensities for the N_2 and N_2^+ bands. It is also worth
24 noting that a He I emission peak at 389 nm can be observed inside the capillary but not outside.
25
26 Another example of a similar trend is for the 677-806 nm window where the relative intensity ratio
27 of the He I to O I is >1 inside the capillary but <1 outside of the capillary. These rough distributions
28 show how the concentration of excited atmospheric species is higher outside the capillary and
29
30
31
32
33
34
35
36
37
38
39
40
41
42
43
44
45
46
47
48
49
50
51
52
53
54
55
56
57
58
59
60

gives an indication of the energy transfer pathways between different plasma species that need to be studied in further detail.

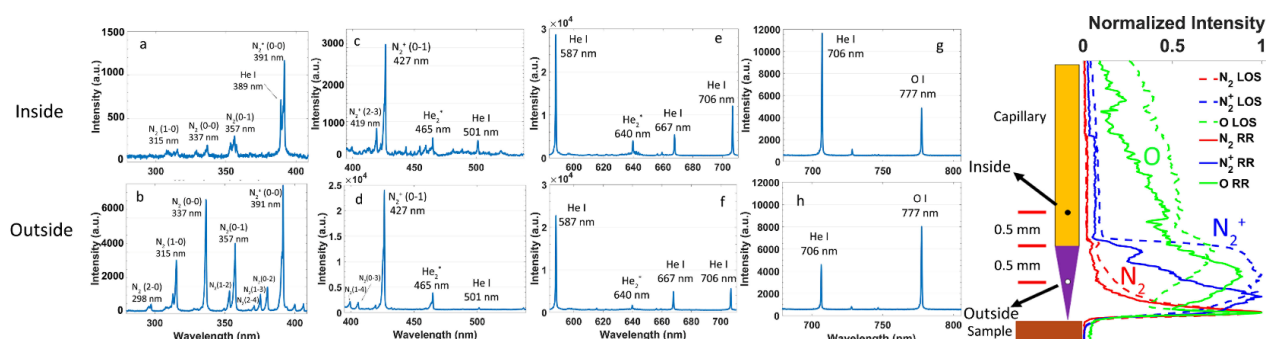


Figure 1. Line-of-sight OES spectra measured at the axis position 0.5 mm inside the capillary (a, c, e, g), and 0.5 mm outside of the capillary (b, d, f, h). The applied voltage is 8 kV and the flow rate is 0.4 L/min. Note that ICCD conditions are different between distinct spectral windows. The image to the right shows plasma axial profiles of LOS vs radially resolved spectral images.

Furthermore, the far right of **Fig. 1** shows a comparison of the normalized axial OES profiles obtained from LOS vs. radially resolved (RR) images. The profile of N_2^+ is significantly different, where the radially resolved data shows the increase in intensity taking place closer to the sample surface compared to the LOS profile. This may indicate that some mechanisms of N_2^+ production may be more significant than previously considered, where only LOS axial profiles were available and used for proposing dominant mechanisms based on the spatial coincidence of increases/decreases in OES intensities from different species³². This also illustrates the importance of obtaining radially resolved information, and that caution should be taken when deducing mechanism based only from LOS images.

Radially resolved optical emission intensity maps

Fig. 2 top shows the radially resolved distribution of He I emission at 706.5 nm, which populates the metastable 3P_2 triplet state $\sim 20.97\text{eV}$ ($3s\ ^3S_1 \rightarrow 2p\ ^3P_{0,1,2}$)³³, under different plasma operating conditions. The dashed lines represent the position of the capillary and the Cu sample

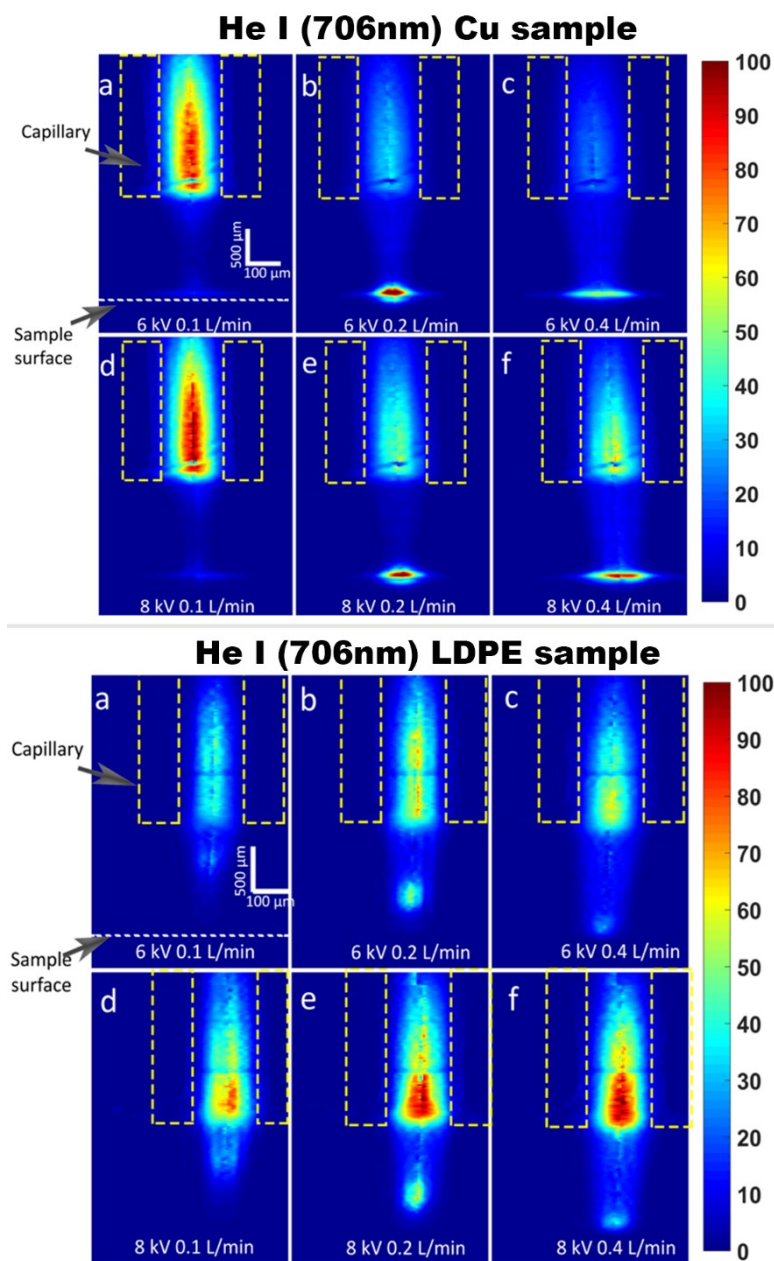


Figure 2. Radially resolved He I (706.5 nm) optical emission intensity maps at varying applied voltage and plasma gas flow rate with a Cu sample (top) and LDPE sample (bottom).

1
2
3 surface. In general, the radial distribution of He I emission shows a convex shape, which has the
4 highest intensity in the axial position. Several emission distribution features can be observed when
5
6
7
8 comparing different conditions. First, the distribution along the axis shows that the intensity is
9
10
11
12
13
14
15
16
17
18
19
20
21
22
23
24
25
26
27
28
29
30
31
32
33
34
35
36
37
38
39
40
41
42
43
44
45
46
47
48
49
50
51
52
53
54
55
56
57
58
59
60

surface. In general, the radial distribution of He I emission shows a convex shape, which has the highest intensity in the axial position. Several emission distribution features can be observed when comparing different conditions. First, the distribution along the axis shows that the intensity is higher inside the capillary and decreases in the open-air region between the capillary tip and the sample surface at 0.1 L/min. However, the intensity increases rapidly again and reaches its maximum at the sample surface at 0.2 L/min, while maintaining a similar trend at 0.4 L/min but with a less intense peak at the sample surface. Second, the overall intensity is slightly higher under the same flow rate when the applied voltage is increased from 6 kV to 8 kV. Third, the intensity inside the capillary decreases significantly (~ 50%) when the flow rate is increased from 0.1 L/min to 0.2 L/min. Note there is a very small region above the edge of the capillary tip where the emission intensity decreases that was confirmed to be a non-transparent feature outside the capillary and can also be observed at other wavelengths.

The bottom of **Fig. 2** shows the radially resolved distribution of He I emission (706.5 nm) with the LDPE sample. Compared with the Cu sample, the most significant difference is the position of the second intensity maximum outside the capillary. For the Cu sample (**Fig. 2** top), the second maximum is at the sample surface under all conditions studied, while for the LDPE it occurs further upstream and moves closer to the surface at higher flow rates. On the other hand, the relative intensity at the surface is much lower with the LDPE sample (**Fig. 2** bottom). In addition, higher flow rates result in higher intensities inside the capillary, in contrast to the opposite trend observed for the Cu sample.

Fig. S3 shows the radially resolved distribution of the He I emission ($3d\ ^3D_{1,2,3} \rightarrow 2p\ ^3P_{0,1,2^0}$) at 587.6 nm with the Cu sample block as the substrate. This transition also populates the 3P_2 triplet state. These images show a similar pattern compared to the 706.5 nm, however, a major difference

1
2
3 is observed inside the capillary, where the intensity is highest at the lowest flow rate for the 706.5
4
5 nm line, but it increases slightly with increased flow rate for the 587.6 nm line. Furthermore, **Fig.**
6
7
8 **S4** shows the radially resolved distribution of He I emission at 388.9 nm ($3p^3P_2 \rightarrow 2s^3S_1$) with
9
10 different plasma operating conditions, in the presence of the Cu sample. The emission images were
11
12 obtained using the 1800 grating in order to enhance the spectral resolution, which allows the He I
13
14 (388.9 nm) line to be resolved from the adjacent N_2^+ 00 first negative system around 391 nm. This
15
16 transition populates the helium metastable atoms in the triplet state (19.82 eV)³⁴. The intensity
17
18 inside the capillary shows a clear trend of decreasing as the flow rate increases, while the intensity
19
20 outside the capillary increases. Unlike the previous two emission species, the 388.9 nm line does
21
22 not have the highest intensity at the plasma/sample interface. Another feature of the emission is
23
24 that the intensity increases from 6 kV to 8 kV, both inside and outside of the capillary.
25
26
27
28

29
30 **Fig. 3** shows the radially resolved distribution of N_2^+ excited species, 0-0 first negative
31
32 system ($B^2\Sigma_u^+ \rightarrow X^2\Sigma_g^+$ transition) at 391 nm³⁵. In the case of the Cu sample (**Fig. 3** top) it is
33
34 evident that the N_2^+ has a much higher intensity in the open-air region between the capillary and
35
36 the sample surface. The overall intensity increases along with both applied voltage and flow rate.
37
38 A noticeable difference compared with the He I emission is that the N_2^+ has lower intensity at the
39
40 axial position, in the region adjacent to the capillary tip. The resulting hollow-cone shape
41
42 distribution surrounds the perimeter of the He I emission (cf. **Fig. 2** top). It is evident that the
43
44 increase of the flow rate promotes the outer layer of the hollow-cone shape to extend closer to the
45
46
47
48
49
50
51
52
53
54
55
56
57
58
59
60

sample surface where a second intensity maximum appears. The trends with LDPE sample (Fig. 3 bottom) are very similar with the absence of the second intensity maximum at the surface.

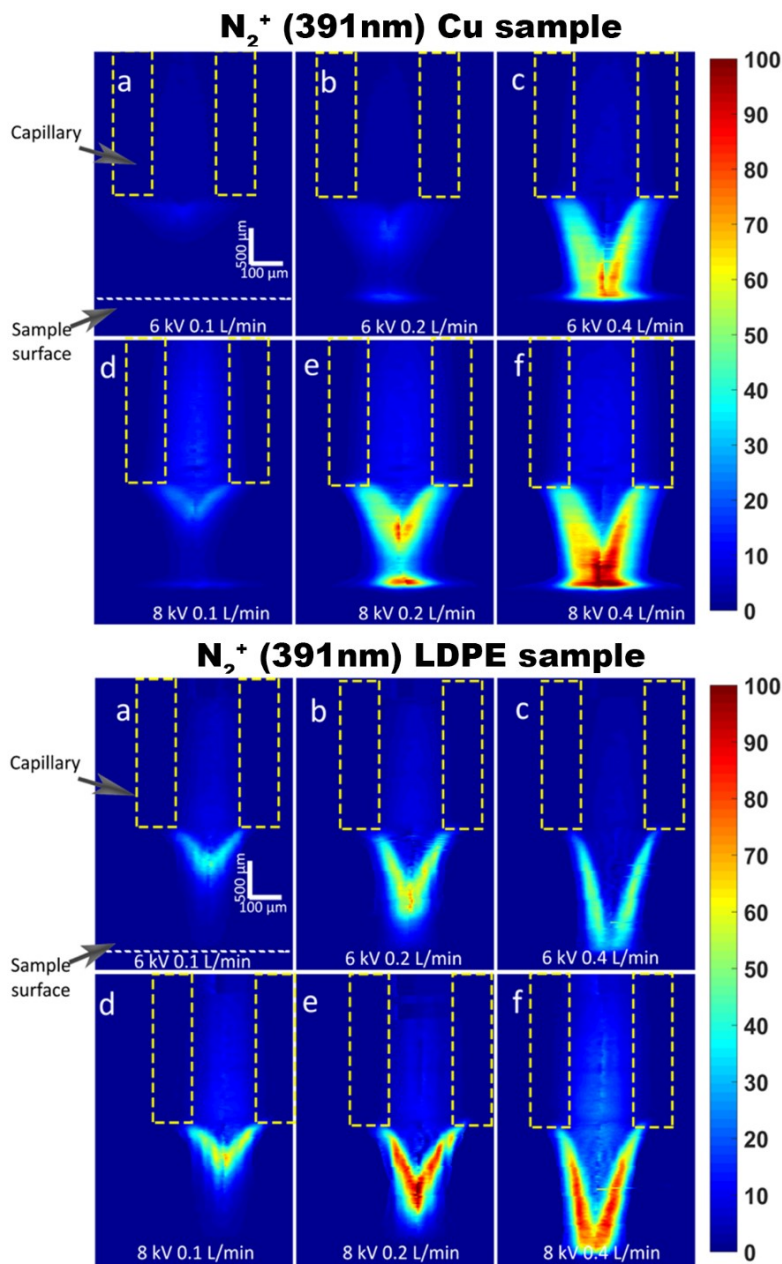
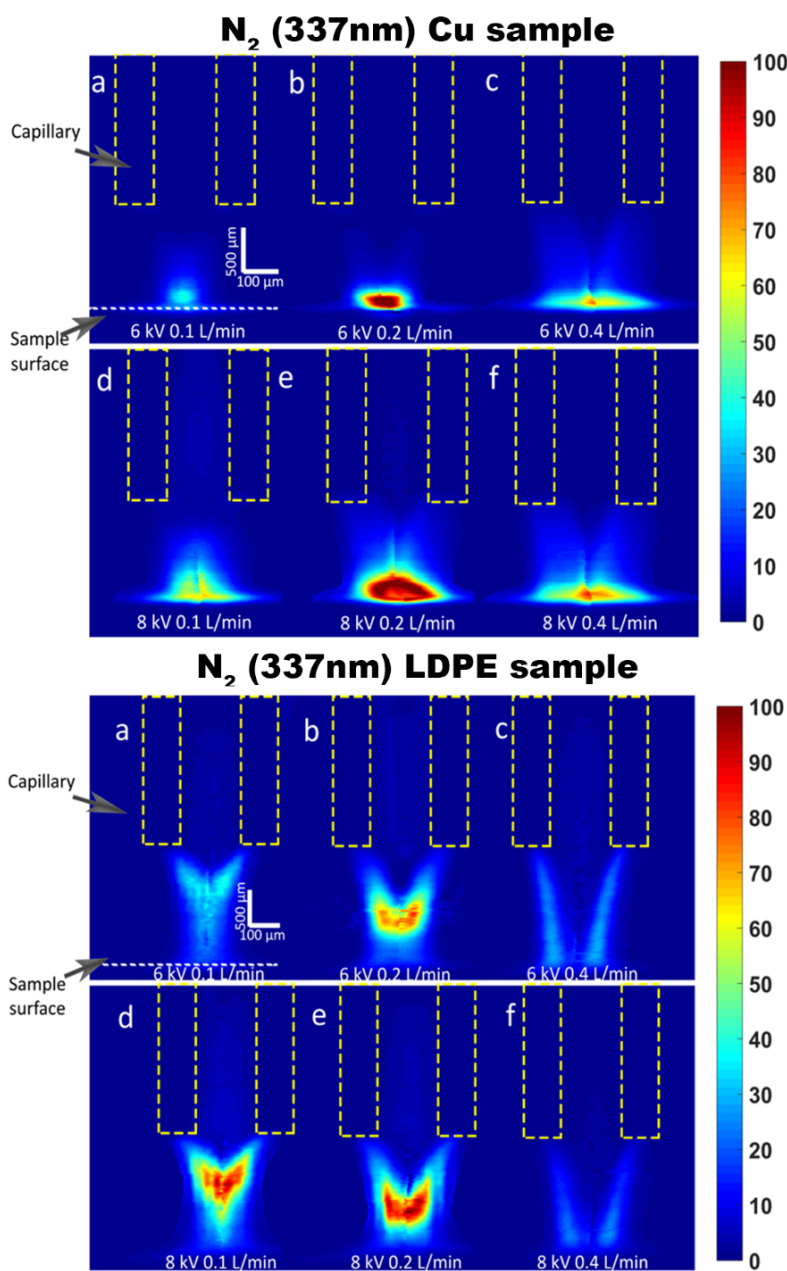


Figure 3. Radially resolved N_2^+ (391 nm) optical emission intensity at varying applied voltage and plasma gas flow rate with a Cu sample (top) and LDPE sample (bottom).

1
2
3 **Fig. 4** shows the radially resolved band head emission of excited N₂, 0-2 second positive
4 system (C ³Π_u → B ³Π_g transition) at 337 nm³⁵. In the case of the Cu sample (**Fig. 4** top), for all
5
6 the plasma operating conditions studied, the intensity of N₂ emission is very low inside of the
7
8
9
10
11
12
13



53 **Figure 4.** Radially resolved N₂ (337 nm) optical emission intensity at varying applied
54 voltage and plasma gas flow rate with a Cu sample (top) and LDPE sample (bottom).
55
56
57
58
59
60

1
2
3 capillary and it increases from the capillary tip towards the sample surface where it reaches its
4
5 maximum. The region of highest intensity is larger when the applied voltage is increased from 6
6
7 kV to 8 kV under the same flow rate. When the flow rate increases, the radial profile changes from
8
9 the convex-shape to the concave-shape, resulting in a hollow-cone distribution, similar to the one
10
11 observed for the N_2^+ emission but with a larger outer radius. The maximum intensity at the sample
12
13 surface peaks at 0.2 L/min and decreases at 0.4 L/min, which is similar to the He I emission
14
15 distribution (c.f. **Fig. 2**). The trends with LDPE sample (**Fig. 4** bottom) have some similarities, but
16
17 significant differences are also clear, such as the hollow-cone shape being evident at the lowest
18
19 flow rate and applied voltage, as well as the absence of the second intensity maximum at the sample
20
21 surface.
22
23
24
25

26
27 **Fig. 5** shows radially resolved OES maps for the He_2^* band head at 640 nm ($d^3\Sigma_u^+ \rightarrow b$
28
29 $^3\Pi_g$ transition). In general, the intensity of He_2^* increases with both the applied voltage and flow
30
31 rate, while there is a slight decrease at 6 kV from 0.2 L/min to 0.4 L/min. It is also very clear that
32
33 increasing the flow rate results in a greater intensity of the emission outside of the capillary
34
35 extending into the open-air region, with a second maximum at the sample surface with higher flow
36
37 rate. The main difference between samples is that the LDPE does not show the second intensity
38
39 maximum at the sample surface.
40
41
42

43
44 **Fig. 6** shows the radially resolved emission intensity distribution of atomic oxygen ($(^4S^o)3p$
45
46 $^5P_{1,2,3} \rightarrow (^4S^o)3p \ ^5S_2^o$ transition) at 777 nm³³. In general, the radial distribution of O I emission
47
48 shows the highest intensity in the axial position and gradually decreases toward the edge of the
49
50 plasma. In the case of the Cu sample (**Fig. 6** top), the emission distribution is similar to the He I
51
52 emission (c.f. **Fig. 2** top) and several features can be observed. First, with a 0.1 L/min flow rate,
53
54 the lateral emission distribution along the axis is higher inside the capillary and it decreases in the
55
56
57

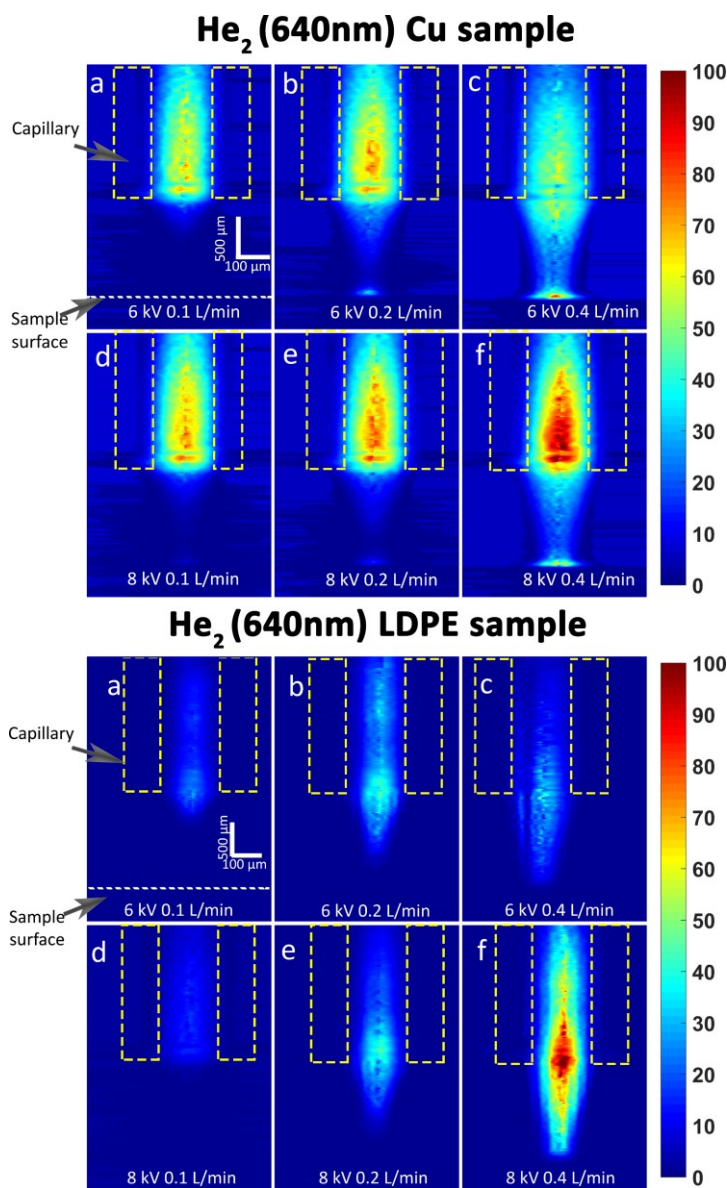
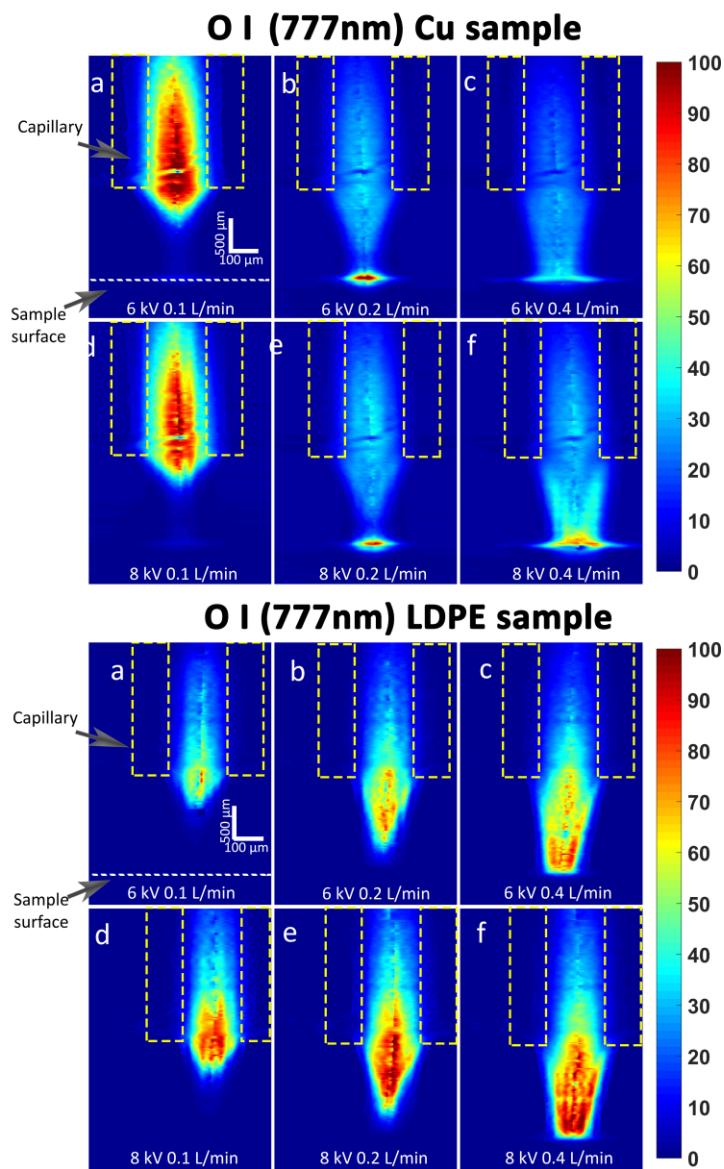


Figure 5. Radially resolved He₂* (640 nm) optical emission intensity at varying applied voltage and plasma gas flow rate with a Cu sample (top) and LDPE sample (bottom).

open-air region between the capillary tip and the sample surface. Second, with 0.2 L/min and 0.4 L/min flow rate, the intensity increases rapidly again near the sample surface, where it reaches its maximum at 0.2 L/min, and then decreases at the highest flow rate. Third, the intensity inside the capillary decreases significantly (~ 55%) from 0.1 L/min to 0.2 L/min. The O I OES maps are significantly different for the LDPE sample (**Fig. 6** bottom). The maximum intensity is always

1
2
3 outside the capillary and it extends further onto the sample with increasing flow rate. In addition,
4
5 the intensity is always higher at increased applied voltage, and there is no maxima anchored at the
6
7 sample surface.
8
9



47 **Figure 6.** Radially resolved O I (777 nm) optical emission intensity at varying applied
48 voltage and plasma gas flow rate with a Cu sample (top) and LDPE sample (bottom).
49
50
51
52
53
54
55
56
57
58
59
60

Vibrational and rotational temperature

Fig. 7 top shows the radially resolved T_{vib} map calculated from Boltzmann plots of the N_2 emission intensity maps under different plasma operating conditions. The uncertainty of the

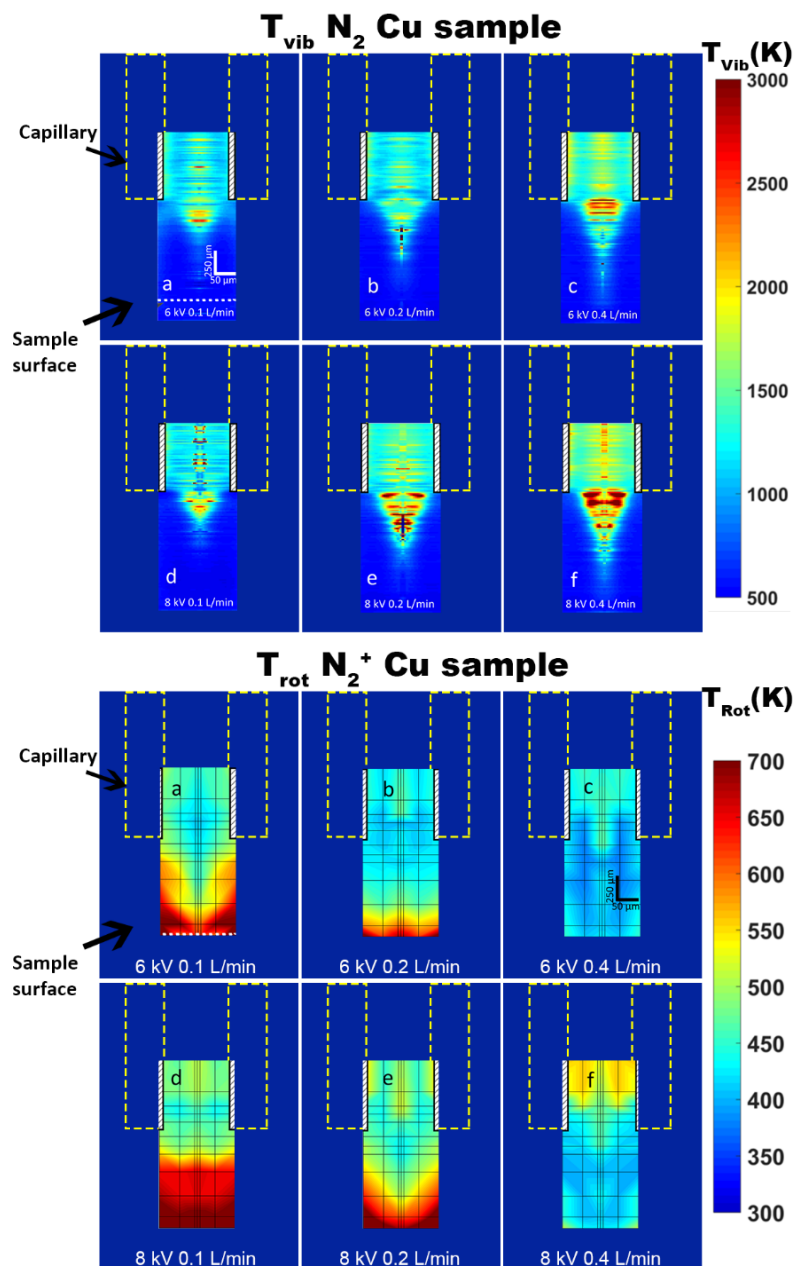


Figure 7. Radially resolved T_{vib} (top), N_2 second positive system ($\text{C}^3\Pi_u \rightarrow \text{B}^3\Pi_g$), and T_{rot} (bottom), N_2^+ first negative system ($\text{B}^2\Sigma_u^+ \rightarrow \text{X}^2\Sigma_g^+$), maps at varying applied voltage and plasma-gas flow rate. The T_{rot} was determined by LIFBASE software fitting of the spectra measured at the cross points of the grid lines and interpolated.

1
2
3 temperature is composed of two parts: the slope fitting error and the measurement precision. The
4
5 propagated uncertainty in the calculated T_{vib} is <12%. The T_{vib} inside the capillary is ~1000 K
6
7 with 6 kV applied voltage and 0.1 L/min flow rate, and it increases with the voltage and flow rate.
8
9 In contrast, the T_{vib} outside of the capillary can reach as high as 3000 K. It is observed that the T_{vib}
10
11 maps show a cone-shape outside of the capillary, which extends further out as the flow rate
12
13 increases. It is also worth mentioning that the temperature decreases rapidly to 500 K at the
14
15 boundary of the cone shape.
16
17
18
19

20 **Fig. 7** bottom shows the radially resolved T_{rot} maps with different plasma operating
21
22 conditions. Note that the T_{rot} maps, as detailed in the experimental section, were determined by
23
24 fitting simulated spectra via LIFBASE software, which makes pixel-by-pixel calculation of the
25
26 T_{rot} very time-consuming. Here, enough spatial positions were selected to construct a temperature
27
28 map via a 2-dimensional linear interpolation algorithm, in an effort to keep a practical image
29
30 processing time. The selected spatial positions are depicted by the grid-line intersection points in
31
32 **Fig. 7** bottom. The uncertainty of the T_{rot} is composed of two parts: the fitting error of the software
33
34 simulation and the measurement reproducibility. The RSD calculated from the Chi-square value
35
36 (χ^2) between the experimental spectra and the simulated spectra is only ~0.5%, while the RSD of
37
38 three replicate acquisitions is ~ 6.5%, which dominates the uncertainty of the T_{rot} . The T_{rot} inside
39
40 of the capillary is around 450 K at 6 kV and increases to about 550 K at 8 kV. At lower flow rates,
41
42 T_{rot} decreases to about 350 K toward the tip of the capillary and then increases near the sample
43
44 surface where it reaches a maximum of ~700 K. As the flow rate is increased, the region of lowest
45
46 temperature is enlarged and the maximum T_{rot} region is constricted toward the sample surface. In
47
48 contrast, at the highest flow rate, 0.4 L/min, it is observed that the region of lower T_{rot} is extended
49
50 even further all the way to the sample surface.
51
52
53
54
55
56
57
58
59
60

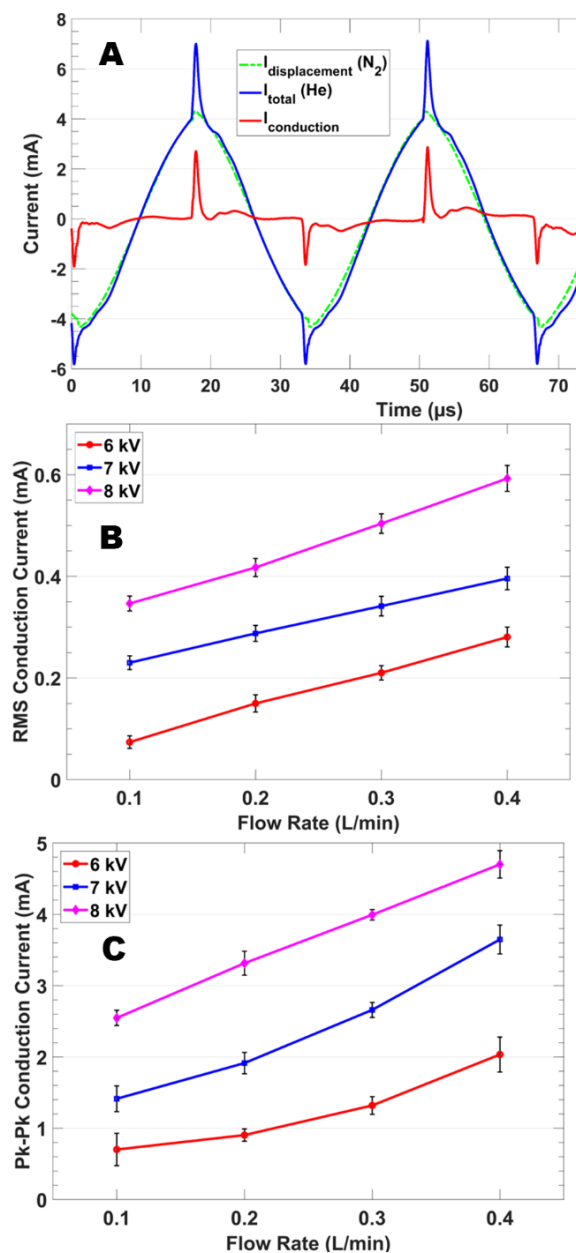


Figure 8. (A) The conduction current of the plasma was calculated by subtraction of displacement current (nitrogen gas, no discharge) from the total current (discharged with helium gas), shown for 8 kV and 0.4 L/min. (B) The RMS and (C) peak-to-peak conduction current as a function of flow rate at different applied voltages.

Electrical characterization

The current measured during plasma operation is the total current (I_{total}) which is composed of two parts: the current flow through the discharge and the current flow through the dielectric²⁵. The displacement current (I_d) represents the current that flows through the dielectric when a different gas replaces the discharge gas and there is no active plasma present. The discharge current, or the conductive current (I_c), can be calculated by the following equation: $I_c = I_{\text{total}} - I_d$.

Fig. 8A shows a selected conduction current waveform, calculated from the plasma total current and the displacement current waveforms. The single discharge peaks shown in each positive and negative cycle indicate the plasma is in homogenous mode that leads to a more even/diffuse distribution of the discharge species, as opposed to a filamentary mode where the plasma species would be concentrated in different filament channels that would manifest as many random current peaks distributed along the waveform³⁶⁻³⁸. **Fig. 8B and 8C** show how the conduction current, both RMS and peak-to-peak, increases with the applied voltage and flow rate.

Crater profilometry

Crater measurement

Fig. 9a shows the profilometry image of the Cu sample surface in contact with μ DBD after 10 min with 8 kV applied voltage and 0.4 L/min helium flow rate. It is clear that a crater is created on the surface, indicating not only desorption, but also erosion occurs on the Cu sample. Notice that the crater bottom is higher than the surrounding positions, showing a convex shape crater.

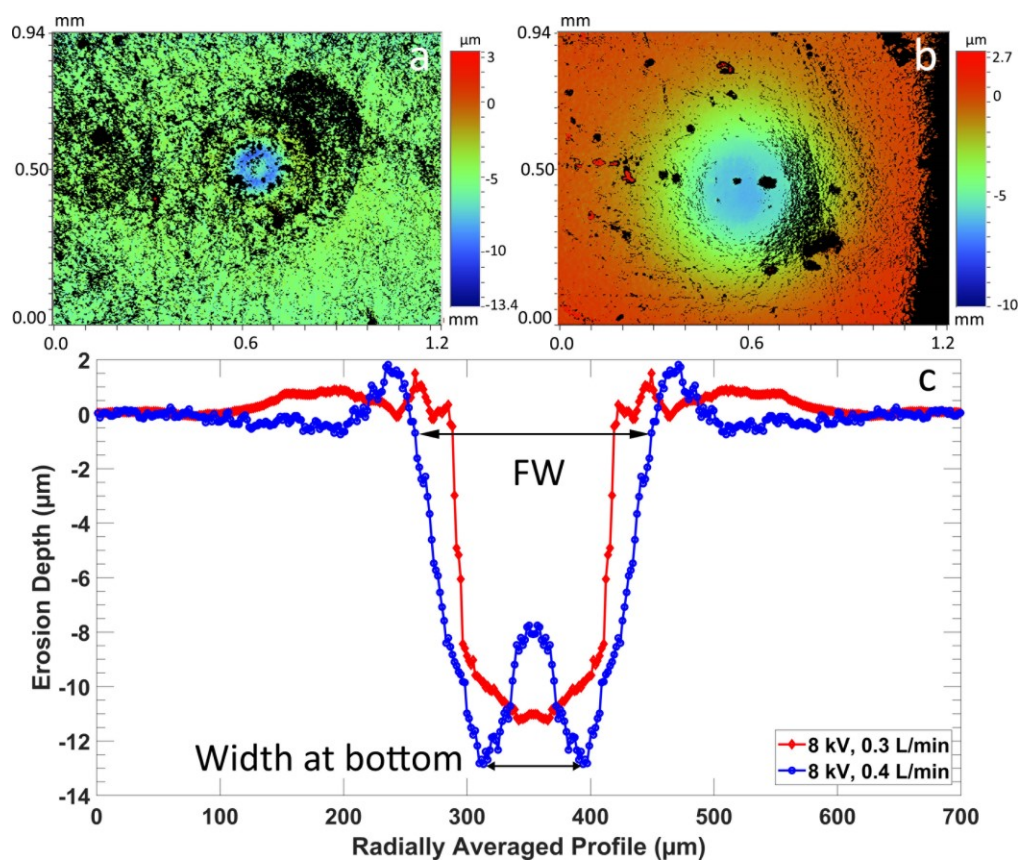


Figure 9. Profilometry images of a) Cu sample and b) LDPE sample. c) Radially averaged cross-section profile of the Cu sample under different flow rates.

In contrast, a much larger but shallower crater is formed on the LDPE surface under the same plasma operation conditions, shown in **Fig. 9b**. Based on the T_{rot} being $>500K$ at the LDPE surface, (calculated in the previous section) the large crater area is most likely due to be by heat transfer from the plasma since the LDPE starts softening after $350K$. **Fig. 9c** shows the radially averaged cross-section profile of the crater. It is evident that the crater shows a convex shape at the bottom (blue line) with $0.4 L/min$ flow rate. However, the convex shape does not exist in other flow rates, i.e., a concave shape bottom (red line) crater is formed with $0.3 L/min$. The possible explanation of the shape of the crater formation will be discussed in the following sections. The full-width at the top, the full-width at half-maximum, and the width at the convex shape bottom (shown in **Fig. 9c**) will be used in the discussion.

Crater shape vs OES images

The plasma-sample surface interaction study is performed via the correlation between the crater shape and the radially resolved OES images. All the emission profiles are extracted at 52 μm (4 pixels) above the sample surface. **Fig. 10a** shows the comparison of full-width of the emission of 5 different plasma species and the full-width at the top of the crater, when the applied voltage is 6 kV. It shows that the N_2^+ emission has the best correlation with the crater full width, with a percentage difference of 4% after averaging all 4 flow rate conditions. The N_2 shows similar trends at 6 kV, with a larger diameter and an average difference of 32%, while the percentage is 39% for He I, 28% for O I, and 35% for He_2 . A similar correlation relationship can be observed with 8 kV applied voltage (**Fig. 10b**). The average difference is 6% for N_2^+ emission, 16% for N_2 emission, and 45~65% for other emissions. As mentioned in the crater characterization section, the crater shows a convex-shape bottom when the flow rate is 0.4 L/min. Therefore, the FWHM of the emission profiles were also compared with the full width of the convex bottom in **Fig. S5**. There is a similar trend of the emission FWHM of nitrogen species with the crater full width, albeit not as clear as with the emission full width.

Discussion

Capillary tip and open-air region

It is commonly believed that the generation of the He atoms excited to metastable levels (19.8 eV or 20.6 eV, denoted He_m), or to a higher excited state (>20.6 eV, denoted He^*), is through the electron-impact mechanism^{33, 34},



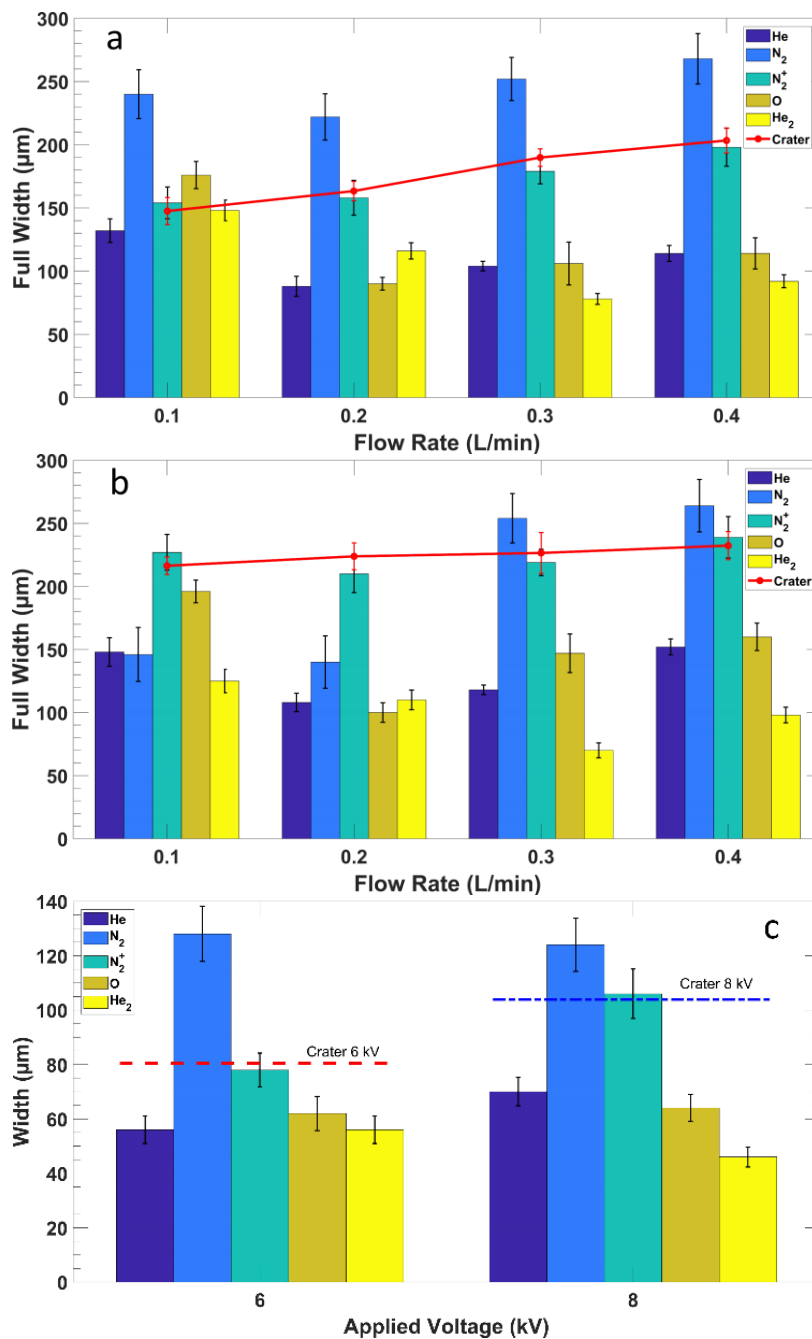
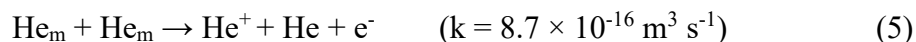


Figure 10. The full width of the radially resolved emission of He, N₂, N₂⁺, O, and He₂ (bar) at 52 μm above the sample surface, compared with the full width at the top of the erosion crater (red line) from 0.1 to 0.4 L/min flow rate. The applied voltage is a) 6 kV and b) 8 kV. c) The FWHM of the emission are compared with the full width of the convex crater bottom with 0.4 L/min flow rate, and 6 or 8 kV voltage applied, respectively. The error bars represent the standard deviation of the triplicate measurements.



and the metastable states have a lifetime in the order of seconds, allowing ionization to occur efficiently³⁹. There are several main routes for the loss of excited helium species with major products of He^+ , He_2^+ , and He_2^* :

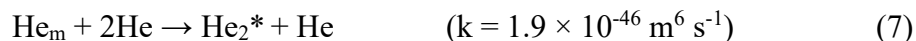
metastable-metastable ionization^{40, 41}:



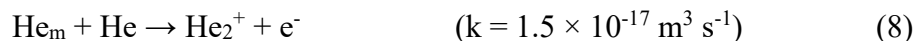
metastable-metastable associative ionization^{40, 41}:



metastable induced association⁴²:



Hornbeck-Molnar associative ionization⁴³:



It is important to take into account the plasma species' residence time in the imaged region. Based on the gas linear velocity (flow rate: 0.1 to 0.4 L/min; capillary i.d.: 150 μm), which is in the range of ~ 100 m/s to 400 m/s, it would take ~ 2.5 μs to 10 μs for the plasma species to traverse this 1 mm region. However, under the 30 kHz AC power conditions used here, there is an ionization wave at each cycle that is faster, for example touching the sample substrate within 10s of ns as reported in⁴⁴. The excited He I species have a very short lifetime and reported energy exchange with other species on the order of ~ 50 ns, which is several orders-of-magnitude shorter than the residence time. Thus, the He I optical emission distributions measured here (**Fig. 2**, 706.5 nm; **Fig. S3**, 587.6 nm, and **Fig. S4**, 388.9 nm) are likely to contain contributions that are representative of regional excitation processes.

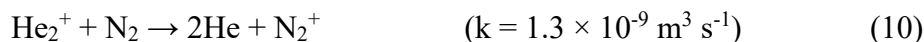
1
2
3 All the He I optical emission maps show a general decrease in intensity inside the capillary,
4
5 along with higher intensity in the region between the capillary and the sample surface, as the flow
6
7 rate is increased. It is possible that the higher linear velocities allow the excited species just inside
8
9 the capillary to travel further downstream before relaxing radiatively. In addition, a larger number
10
11 density of higher energy electrons may be available further downstream at higher flow rates, such
12
13 that electron impact excitation (Eq. 3) can take place more efficiently. This is supported by the
14
15 measured distribution trends of T_{vib} (c.f. **Fig. 7**, given that these N_2 transitions typically arise from
16
17 electron impact processes and are thus indicative of T_e), where the cone-shaped tail region of
18
19 higher T_{vib} extends further outward and displays higher temperatures at increased flow rates. Further
20
21 et al.⁴⁵ also measured a rise in the T_{vib} at increased voltages or flow rates on a larger sized DBDI
22
23 source than used here (2 mm o.d.). Furthermore, all the He I transitions measured here populate
24
25 metastable states, which would indicate that the He metastable number density surges further
26
27 downstream from the capillary as the flow rate is increased. This agrees with studies by Farnsworth
28
29 et al. where the He metastable density in an APPJ, measured via laser-induced fluorescence (LIF),
30
31 is reported to rise further away from the capillary tip as the flow rate is increased⁸.

32
33 Also, it is interesting to note that the radially resolved imaging allows the observation of
34
35 the cone-shaped tail formed by the He I optical emission being followed downstream by the
36
37 hollow cone-shaped optical emission of the N_2^+ (c.f. **Fig. 3**). The nitrogen molecular ion (N_2^+)
38
39 plays an important role in APPJs flowing into air, as it is generally agreed that N_2^+ is responsible
40
41 for the formation of the protonated water clusters, which are known ionization reagents of
42
43 interest⁴⁶⁻⁴⁸. Qayyum et al. reported that the transitions related to the N_2^+ first negative system (B
44
45 $2\Sigma_u^+ \rightarrow \text{X } 2\Sigma_g^+$ transition) cannot be initiated in a pure nitrogen plasma at atmospheric pressure.
46
47 However, the transition is almost resonant in the helium-based ambient ionization source⁴⁹.

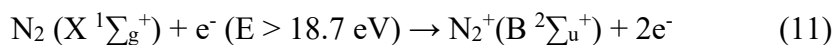
There are three major reaction routes for the N_2^+ formation from the neutral ambient nitrogen gas. First, via Penning ionization (PI) with the helium metastable^{48, 50}



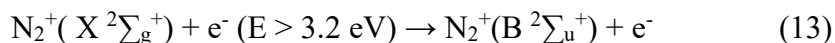
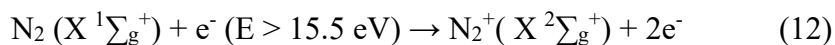
Second, via charge transfer (CT) with the helium dimer ion^{46, 51}:



Third, via direct electron excitation with high-energy electrons. It is possible to perform the ionization and excitation at the same time through a one-step process⁵²:



Or it may go through the ionization and excitation separately with a two-step process⁵³:

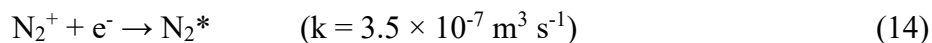


The spatial coincidence of the He I emission profile upstream and the N_2^+ emission profile downstream indicates that PI plays an important role, as reported by Chan et al.³² for a larger DBD under typical desorption/ionization conditions, given that the He I transitions measured populate metastable states. This is further supported by the measured T_{rot} distribution (c.f. **Fig. 7**). PI (Eq. 9) and CT (Eq. 10) reactions can produce excited nitrogen molecular ions, but the population of the resulting rotational states are different, which manifests as different T_{rot} . It is reported that the PI pathway can yield a rotational temperature of $360 \pm 30 \text{ K}$, while the CT pathway can yield $900 \pm 60 \text{ K}$ ^{54, 55}. Therefore, at lower flow rates, the lower temperature region observed just outside the capillary is indicative of PI, while the much higher temperature region closer to the sample surface is indicative of CT. Moreover, increases in flow rate result in the higher temperature region

1
2
3 shrinking toward the sample surface until it disappears at the highest flow rate, which correlates
4 with the higher intensities of the He I optical emission (transitions into He metastable states)
5 increasing toward the sample surface at higher flow rates. It is interesting to note that while the
6 T_{rot} decreases with flow rate, the intensity of the N_2^+ band head at 391 nm increases, showing a
7 surge in excited N_2^+ , even when the concentration of N_2 from air diffusing into the same area
8 should be lower. This is not just a shift in the populated levels, as indicated by the T_{rot} , because
9 the spatial profile of the N_2^+ optical emission and the T_{rot} changes do not coincide (cf. **Fig 3** and
10 **Fig 7**, 8 kV and 0.2 L/min). It is worth noting that the plasma gas used, He UHP, does have a
11 reported N_2 impurity content of 5 ppm, according to the manufacturer. It is also interesting to note
12 that an increase of applied voltage or flow rate will lead to an increase of the plasma conduction
13 current (c.f. **Fig. 8**), suggesting that there will be more charged species present in the plasma. This
14 correlates well with the trends of the N_2^+ band head emission at 391 nm.
15
16
17
18
19
20
21
22
23
24
25
26
27
28
29

30 *Plasma plume/surface interface*

31
32
33
34 In the absence of a nearby sample surface, the N_2 optical emission peak appears just
35 downstream of the N_2^+ (**Fig. S7**), which confirms the results of Chan et al. for a larger DBD
36 under typical ambient mass spectrometry conditions³². Here, the radially resolved imaging
37 allows the observation of the axial and radial structure of this sequence when the μDBD plasma
38 plume is exposed to the isolating LDPE sample surface (c.f. **Fig. 3** and **Fig. 4**). It is also evident
39 that a full cone-tail shaped N_2 optical emission is observed at lower flow rates and is pushed
40 closer toward the sample surface as the flow rate is increased, until the tip is no longer observed,
41 but only the edges. The spatial distribution relationship between the excited N_2 and the N_2^+
42 suggests that the energy of the excitation is likely to come from a recombination mechanism with
43 the excited nitrogen ion species, as proposed in ^{32, 56}.
44
45
46
47
48
49
50
51
52
53
54
55
56
57
58
59
60



On the other hand, a very significant difference is observed in the N_2 optical emission distribution when the plasma plume is exposed to the copper sample, where the maximum intensity is always at the sample surface regardless of the voltage/flow rate settings. In fact, the optical emission of every plasma species imaged here displays a peak at the plasma/copper sample interface, particularly as higher voltages and flow rates. In contrast, exposing the plasma plume to the LDPE sample does not result in such emission peaks at the surface. The plasma optical emission spatial structure is pushed outward at higher flow rates but seems to be cut-off, or extinguished, at the LDPE surface. This phenomenon shows that the sample surface nature plays a critical role in the underlying mechanisms and is not just a passive component, which is of great significance toward plasma-based ambient desorption/ionization applications. These differences may arise from several factors, including the polymer additives and fragments interacting with the plasma plume. Another significant difference is that the LDPE is an isolating surface, while the copper, even when it is not grounded but floating, presents a much more efficient charge reservoir/well.

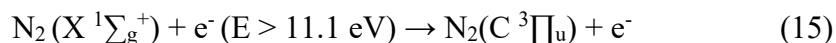
Some effects of exposing the plume of an APPJ to a nearby surface have been previously described. For example, Farnsworth et al. showed that the presence of a glass slide surface 10 mm downstream of a He DBD resulted in an increase of the measured He metastable population at 4 mm downstream⁸. This agrees with the results here, where exposing the plasma plume to the LDPE sample resulted in an emission peak of the He I (706.5 nm), which populates a metastable state, between the sample surface and the capillary tip (c.f. **Fig. 2**). Zaplonik et al. measured the 2^3S_1 He metastable density in the plume of a single electrode APPJ and found that it increased up to 10x in the presence of a sample surface, which also correlates with its conductivity⁵⁷. In addition, they

1
2
3 showed the He metastable density increased at a Fe sample surface placed 1 mm – 5mm
4 downstream. This also agrees with the He I optical emission image at 388.9 nm observed here,
5
6 which populates the 2^3S_1 He metastable level, that peaks at the copper sample surface (c.f. **Fig.**
7
8 **S4**), as well as the other He I transitions measured (c.f. **Fig. 2** and **Fig. S3**).
9
10
11

12
13 Kushner et al. performed plasma hydrodynamics modeling, nonPDPSIM, on a He/O₂
14 (99.8/0.2) APPJ, flowing into humid air and impinging on a thin varying dielectric ($\epsilon/\epsilon_0 = 2$, similar
15 to LDPE, to 80) or metallic surface⁴⁴. It is worth noting that in their model the APPJ was pulsed
16 to 80 ns and their results are temporally resolved. They note that the ionization wave (IW),
17 propagating from the APPJ onto the surface, is faster in the case of the metal substrate and it yields
18 a higher T_e and n_e , as well as ion density. They also report an increase in the densities of certain
19 neutrals, e.g. excited He I (including 2^3S metastables) and excited N₂, in the metal surface case,
20 while citing the charging of the lower ϵ_r dielectric surface as partly responsible for their lower
21 reported densities of excited neutrals. They observe the metal surface causing a return stroke that
22 sustains the discharge for a longer time after the IW first impacts the surface. On the other hand,
23 the dielectric surfaces promote the formation of surface ionization waves (SIW) radiating outward
24 from the plasma axis, as a consequence of the fast surface charging and the horizontal electric field
25 component that sustain them, along with a fast decrease of the vertical electric field component.
26
27 Sobota et al. measured the T_e and n_e via Thomson scattering, as well as the densities and
28 temperatures of O₂ and N₂ via Raman scattering, on a He APPJ (6 kV, 1 μ s unipolar positive pulses
29 at 5kHz) flowing into air while exposing the plume to various target surfaces⁵⁸. They report a
30 significant rise in n_e (~30% to 300%) and T_e (~20% to 200%) just above the target (glass < water
31 < copper), compared to the free-flowing plume case, during the start of the power pulse (-20 ns to
32 +130 ns). Furthermore, in the case of the copper target, they were able to measure larger increases
33
34
35
36
37
38
39
40
41
42
43
44
45
46
47
48
49
50
51
52
53
54
55
56
57
58
59
60

1
2
3 in n_e and T_e , as well as T_{rot} until 1.25 μs after the start of the power pulse. The authors report a
4
5 diffuse discharge sustained above the copper target following the return stroke and propose that
6
7 secondary electrons from ions impacting the surface are the source of electrons, taking into account
8
9 that the copper target is floating.
10
11

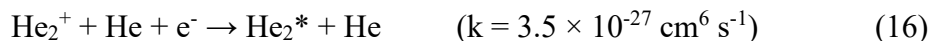
12
13 Regarding the results herein, the peak in the He I optical emission intensities observed at
14
15 the surface of the copper target indicate that more efficient electron impact excitation (Eq. 3 and
16
17 4) can take place in this region, supported by the higher T_e and n_e reported near the copper surface⁵⁸.
18
19 It is highly probable that this is also the case for the other plasma species whose optical emission
20
21 intensity peaks at the copper surface. It is particularly interesting for N_2 because in the case of the
22
23 free-flowing plasma plume, excitation is mainly through recombination reactions, as discussed
24
25 above (Eq. 14) and further indicated by the spatial sequence with N_2^+ optical emission. While this
26
27 spatial coincidence is still there in the case of the LDPE target, this is no longer the case at the
28
29 copper target surface, which indicates that a different excitation mechanism of the N_2 state ($C^3\Pi_u$)
30
31 is taking place, such as direct electron-impact excitation⁵².
32
33
34
35



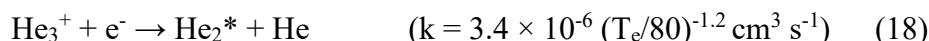
36 37 38 39 ***Excited Helium Dimer***

40
41
42 Optical emission from the excited helium dimer He_2^* , or excimer, is observed at 464 nm
43
44 and 640 nm⁵⁹ (c.f. **Fig. 1** c-f). Hill et al. reported that for the He dimer molecules, the singlet states
45
46 are unstable with a radiative decay in several nanoseconds⁶⁰. However, the triplet state molecules
47
48 are “metastable” with a radiative lifetime of seconds due to a strongly forbidden spin flip required
49
50 for the radiative transition to the ground state of two free atoms⁶¹.
51
52
53
54
55
56
57

Besides metastable induced association (Eq. 7), there are other proposed mechanisms for the generation of the excited helium dimer, for example, the dissociative recombination reaction of helium molecular ion:⁶²



or the dissociative recombination reaction of helium He_3^+ ion:^{63, 64}



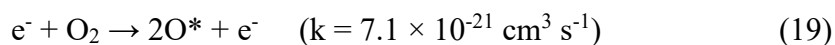
Note that the presence of He_3^+ has been detected in high-pressure discharges, but it is a not very stable molecule and Eq. 18 is T_e dependent with a very fast reaction rate when the T_e is close to room temperature³⁴.

With respect to the role of He_2^* , it has been argued to be unimportant mainly from two aspects: first, the energy of He_2^* is lower than the sum of the ionization and excitation energy of the N_2 ($X^1\Sigma_g^+ \rightarrow B^2\Sigma_u^+$ transition, 18.7 eV) and secondly the number density of He_2^* are reported lower than He_m^* in both vacuum⁶⁵ and atmospheric⁶⁶ environments. Nonetheless, the observations in this study indicate that He_2^* may play a more significant role than previously thought in the energy transfer pathways. First, according to Eq. 12 and Eq.13, the $\text{N}^2 X^1\Sigma_g^+ \rightarrow \text{N}_2^+ B^2\Sigma_u^+$ transition can be accomplished in a two-step process if the energy requirement is met. The lowest triplet helium excimer He_2^* ($a^3\Sigma_u^+$) has an energy of 18.1 eV⁴³, which is high enough for either ionization (15.5 eV) or excitation (3.2 eV) of N_2 ⁵². Second, the results in **Fig. 1** show that the emission intensity ratio of the He I (587.6 nm)/ He_2^* (640 nm) is less than 10 inside the capillary (**Fig. 1e**) but around 22 outside of the capillary (**Fig. 1f**), mainly from a decrease in He_2^* intensity. The increase of the ratio suggests a higher helium excimer loss occurring, thus contributing to the

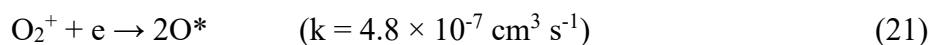
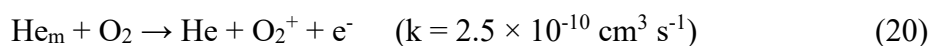
energy transfer. Third, the radially resolved emission of He₂* shows a similar distribution compared to He I, which correlates well to the distribution of N₂⁺.

Processes Involving Oxygen

Regarding the O I emission at 777 nm (c.f. **Fig 6**), it is important to note the differences when the plasma plume is exposed to a copper vs LDPE sample. It is generally agreed that the atomic oxygen is dominant over molecular oxygen in the atmospheric pressure discharge due to the breakdown of the molecules in the plasma through electron-impact dissociation⁶⁷.



Another possible pathway for atomic oxygen generation is through Penning ionization followed by dissociative recombination of O₂⁺ ions:⁶⁸



In the case of the copper sample, electron-impact dissociation may play a more significant role, taking into account the similarities with the He I OES distribution and the higher T_e and n_e modeled in⁴⁴ and measured in⁵⁸, particularly at the plasma/sample interface. On the other hand, the LDPE sample would have much lower T_e and n_e, which would mean that Penning ionization would be a more significant mechanism. In addition, with the LDPE sample, it is interesting to note that the region of higher O I optical emission grows toward the sample surface as the flow rate is higher. This indicates that atomization/excitation mechanisms are significantly higher, because there is a lower amount of ambient air allowed to mix at higher flow rates, which would result in lower O₂ concentrations in this region. It is important to also consider that atomic oxygen will diffuse faster

1
2
3 compared to its molecular counterpart. In addition, it is worth noting that the plasma gas used, He
4 UHP, does have a reported O₂ impurity content of 1 ppm, according to the manufacturer. In
5
6 contrast, the copper sample has a higher O I optical emission intensity inside the capillary at the
7
8 lowest flow rate, which changes to a peak found at the sample surface when using higher flow
9
10 rates. In this case, however, another mechanism called helium channeling may be changing the O₂
11
12 concentration originating from air, as reported for an APPJ impinging on metallic substrates⁶⁹,
13
14 where the ion drag force results in a higher purity helium channel extending to the surface.
15
16
17
18
19

20 Furthermore, the oxygen may have an additional role in the resulting He metastable
21
22 production. Winter et al. showed the He metastable distribution in the plasma plume of a helium
23
24 APPJ (axial pin electrode, V_{pp} 1.76 kV at 940 kHz AC) was significantly affected by the O₂/N₂ of
25
26 the surrounding gas⁷⁰. In short, the measured He metastable density was highest (~1 x 10¹³ cm⁻³)
27
28 with an 80% O₂/20% N₂ sheath gas composition, lower for 100% O₂, significantly lower for 5%
29
30 O₂/95% N₂, and below their detection limit (~1 x 10¹³ cm⁻³) for 100% N₂. They observe similar
31
32 trends when N₂ is replaced by Ar and attribute the lower He metastable density to the absence of
33
34 O₂, rather than the increase in N₂. Kushner et al. then used temporally resolved OES imaging with
35
36 bandpass filters, for N₂ (390nm center, 20nm FWHM) and He (707nm center, 7nm FWHM)
37
38 species, as well as a plasma hydrodynamics computational model, non-PDPSIM, to study the
39
40 effect of the surrounding gas composition in the same type of APPJ plume⁷¹. They found that
41
42 during the positive half cycle, the emission travels from the ambient air toward the jet nozzle,
43
44 against the gas flow, when the shielding gas contains O₂. Their modeling results showed that when
45
46 O₂ is in the shielding gas, an anion sheath surrounds the He channel and allows the IW to travel
47
48 further, together with higher electric fields at the front, which results in the higher metastable
49
50
51
52
53
54
55
56
57
58
59
60

1
2
3 density. Thus, similar processes may be sustained in the uDBD APPJ studied here, but further
4
5 temporally resolved OES imaging studies are needed to confirm this.
6
7

8 *Surface Sampling*

9

10
11 Finally, it is important to consider the material surface sampling/etching mechanisms that
12
13 may take place. Etching with plasma jets is typically implemented with reactive gases (e.g. CF₄ or
14
15 SF₆) and on materials such as silicon or polymers⁷². However, there are several reports of APPJs
16
17 with He/O₂ plasma gas flowing into ambient air for polymer etching⁷³. In this case, the UV
18
19 photons, electron impact and reactive oxygen species, such as O or OH, contribute to dissociation
20
21 of molecules in the polymer, as well as formation of surface radicals that serve as starting points
22
23 for the etching process⁷⁴. The high intensity O I optical emission region observed here for the
24
25 LDPE sample (c.f. **Fig. 6**) points to the significance of such mechanisms. Furthermore, the peak
26
27 T_{rot} observed (~700K) toward the sample surface would not only enhance the etching process but
28
29 may also contribute to thermal-based effects, such as melting, since softening of LDPE starts
30
31 ~350K, which probably leads to the large size of the craters observed in the LDPE sample (c.f. **Fig**
32
33 **9b**). On the other hand, the craters measured in the copper sample are much smaller (c.f. **Fig. 9a**)
34
35 and there was a clear correlation of the N₂⁺ optical emission and the crater full width, or in the case
36
37 of ring-shaped bottom craters, a correlation of the N₂⁺ optical emission FWHM and the valley-to-
38
39 valley distance (c.f. **Fig. 10**). APPJs are not typically used for metal etching, but mostly metal
40
41 surface treatment, such as hydrophilic/hydrophobic modification⁷². However, Kuwahata and
42
43 Yamaguchi showed that an Ar DBD-based APPJ flowing into open air could be used for removing
44
45 Al thin films deposited on glass slides⁷⁵. On one hand, they observe streamers from the APPJ that
46
47 converge onto the sample surface and result in concave shaped craters at longer APPJ/surface
48
49 distances. On the other hand, at shorter APPJ/surface distances, they observe the streamers
50
51
52
53
54
55
56
57
58
59
60

1
2
3 maintain the original ring-shaped structure they display flowing along the wall of the APPJ quartz
4 tube, which results in ring-shaped craters. In our study here, a similar process may be taking place,
5 supported by the crater shapes changing from concave to ring-shaped as the flow rate is increased,
6 which in turn results in pushing the plasma plume OES spatial structure onto the sample surface,
7 thus having a similar effect as bringing the APPJ tube closer to the sample surface. Again, further
8 temporally resolved OES imaging diagnostic studies are needed to confirm this and explain the
9 correlation between the N_2^+ emission and the resulting crater shape.
10
11
12
13
14
15
16
17
18
19
20
21
22

23 **Conclusions**

24
25
26 In this study, radially resolved OES plasma diagnostics on a He μ DBD flowing onto
27 different sample materials in the open air were successfully performed. The measured radially
28 resolved distribution maps of representative plasma species (He I, N_2^+ , N_2 , He₂, O I) provided
29 insights into energy transfer pathways and display clear differences compared to their line-of-sight
30 counterparts, thus showing the importance of radially resolved data. The electrical studies results
31 show that higher applied voltage or discharge gas flow rate leads to a higher conduction current,
32 indicating more charged species are present in the active plasma region.
33
34
35
36
37
38
39
40
41
42

43 The main goal of this study was achieved by obtaining further insights into the underlying
44 mechanisms changes brought upon exposing the APPJ plasma plume to different sample surfaces.
45 The OES spatial distribution sequences between the different plasma species monitored, show that,
46 when the plasma plume impinges on an LDPE target, similar energy transfer pathways are
47 observed compared to its free-flowing counterpart. This means that in the upstream region of the
48 He μ DBD, N_2^+ is produced by PI with He metastables, while downstream they are produced by
49
50
51
52
53
54
55
56
57
58
59
60

1
2
3 CT with He_2^+ , as supported by the T_{rot} maps, followed by electron recombination to yield excited
4
5 N_2 . On the other hand, the OES spatial structure of the plasma plume changes significantly when
6
7 it interacts with a floating copper sample, particularly at the plasma/surface interface where most
8
9 species display an intensity peak. This is proposed to be due to an increased T_e and n_e close to the
10
11 sample surface, which promotes electron impact excitation, that is in turn due to a faster ionization
12
13 wave during the start of the positive half-cycle and the subsequent return stroke, followed by a
14
15 diffuse glow-like discharge in the presence of a metal target and not observed in non-conductive
16
17 targets, as reported for other APPJ configurations.
18
19
20
21

22
23 Interestingly, a clear correlation between the widths of the erosion crater in the copper
24
25 sample and the N_2^+ emission was observed, which indicates the nitrogen ion could play an
26
27 important role in the surface erosion process and may be utilized for monitoring of such processes.
28
29 Moreover, the presence of streamers originating in the plasma are proposed to be involved in the
30
31 erosion process, as reported for other APPJ configurations. In addition, future studies including
32
33 spatiotemporally resolved OES maps, as well as fundamental parameters maps, e.g. T_e and n_e , are
34
35 underway to provide further insight/confirmation into some of the proposed underlying
36
37 mechanisms.
38
39
40

41
42 It is worth noting that the observations here may be applicable to other APPJs, e.g. the
43
44 ones typically utilized for plasma-based ambient desorption/ionization mass spectrometry,
45
46 biomedical applications, surface modifications, etc⁷⁶. For example, low-temperature plasma (LTP),
47
48 a DBD APPJ, MS method development studies have shown that the negative ion mass spectral
49
50 fingerprints of chemical warfare agents are significantly changed when desorbed from different
51
52 substrates⁷⁷. Specifically, a higher degree of fragmentation was observed when analyzing TNT
53
54 (2,4,6-trinitrotoluene) on copper foil in comparison to a glass slide (seen by a significant ratio
55
56
57
58
59
60

1
2
3 change between the [M-H]⁻ peak at m/z 226 and a fragment ion [M-H-NO]⁻ peak at m/z 197). This
4
5 is in line with our results presented here, particularly the increased optical emission intensities near
6
7 the Cu sample surface, but absent in the PTFE sample, with their proposed origin being attributed
8
9 to an increase of the n_e and T_e , which would in turn result in higher degree of analyte fragmentation.
10
11 However, plasma-based AMS studies on the effect of different substrates have typically focused
12
13 on improvements in LODs and other analytical figures of merit^{77, 78}, rather than mechanistic ion
14
15 formation. Therefore, there is a need to study the effect of various substrates on the underlying
16
17 mechanisms responsible for MS ion formation, especially in regards to APPJs used for chemical
18
19 analysis applications (e.g. μ DBDs), which are the focus of current and future studies in our
20
21 laboratory.
22
23
24
25
26
27
28
29

30 Acknowledgments

31
32 The authors would like to acknowledge support by the National Science Foundation under
33
34 CHE-1610849.
35
36
37

38 References

- 39
40
41 1. D. R. Baer, *Surface and Interface Analysis*, 2012, **44**, 1305-1308.
42 2. P. M. Peacock and C. N. McEwen, *Analytical Chemistry*, 2004, **76**, 3417-3428.
43 3. T. Gruending, S. Weidner, J. Falkenhagen and C. Barner-Kowollik, *Polymer Chemistry*,
44 2010, **1**, 599-617.
45 4. S. M. Weidner and S. Trimpin, *Analytical Chemistry*, 2010, **82**, 4811-4829.
46 5. Z. Takáts, J. M. Wiseman, B. Gologan and R. G. Cooks, *Science*, 2004, **306**, 471.
47 6. M. C. Jecklin, G. Gamez and R. Zenobi, *Analyst*, 2009, **134**, 1629-1636.
48 7. Z. Xing, J. Wang, G. Han, B. Kuermaiti, S. Zhang and X. Zhang, *Analytical Chemistry*, 2010,
49 **82**, 5872-5877.
50 8. M. S. Heywood, N. Taylor and P. B. Farnsworth, *Analytical Chemistry*, 2011, **83**, 6493-6499.
51 9. K. Sasaki, R. Engeln and E. V. Barnat, *Journal of Physics D: Applied Physics*, 2018, **51**.
52 10. M. Šimek, *Journal of Physics D: Applied Physics*, 2014, **47**.
53 11. L. Hood-Hong, *Journal of Science and Technology*, 2014, **6**.
54 12. M. A. Song, Y. W. Lee and T. H. Chung, *Physics of Plasmas*, 2011, **18**, 023504.
55
56
57
58
59
60

13. V. Laporta and D. Bruno, *J Chem Phys*, 2013, **138**, 104319.
14. G. C. Y. Chan and G. M. Hieftje, *Spectrochimica Acta Part B: Atomic Spectroscopy*, 2006, **61**, 31-41.
15. S. H. Nam and Y. Jo Kim, *Bulletin of the Korean Chemical Society*, 2001, **22**, 827-832.
16. J. M. Palomares, S. Hübner, E. A. D. Carbone, N. De Vries, E. M. Van Veldhuizen, A. Sola, A. Gamero and J. J. A. M. Van Der Mullen, *Spectrochimica Acta - Part B Atomic Spectroscopy*, 2012, **73**, 39-47.
17. S. Shi, X. Gong, Y. Mu, K. Finch and G. Gamez, *Journal of Analytical Atomic Spectrometry*, 2018, **33**, 1745-1752.
18. S. Shi, K. Finch, Y. She and G. Gamez, *Journal of Analytical Atomic Spectrometry*, 2020, **35**, 117-125.
19. M. Kroschk, J. Usala, T. Adesso and G. Gamez, *Journal of Analytical Atomic Spectrometry*, 2016, **31**, 163-170.
20. G. Gamez, D. Frey and J. Michler, *J. Anal. At. Spectrom.*, 2012, **27**, 50-55.
21. C. A. Schneider, W. S. Rasband and K. W. Eliceiri, *Nature Methods*, 2012, **9**, 671-675.
22. H. D. Yang, K. X. Chen, Q. S. He and G. F. Jin, *Spectroscopy and Spectral Analysis*, 2009, **29**, 3169-3172.
23. C. Pernechele, L. Poletto, P. Nicolosi and G. Naletto, *Optical Engineering*, 1996, **35**, 1503-1510.
24. G. Pretzler, *Z. Naturforsch. Sect. A-J. Phys. Sci.*, 1991, **46**, 639-641.
25. Y. Hong, N. Lu, J. Pan, J. Li and Y. Wu, *Thin Solid Films*, 2013, **531**, 408-414.
26. F. J. Gordillo-Vázquez, M. Camero and C. Gómez-Aleixandre, *Plasma Sources Science and Technology*, 2005, **15**, 42-51.
27. N. U. Rehman, A. Masood, Z. Anjum, I. Ahmad, M. A. Khan and M. Zakaullah, *Radiation Effects and Defects in Solids*, 2015, **170**, 668-678.
28. A. N. Goyette, W. B. Jameson, L. W. Anderson and J. E. Lawler, *Journal of Physics D: Applied Physics*, 1996, **29**, 1197-1201.
29. A. N. Goyette, J. R. Peck, Y. Matsuda, L. W. Anderson and J. E. Lawler, *Journal of Physics D: Applied Physics*, 1998, **31**, 1556-1564.
30. P. W. J. M. Boumans, 1987.
31. J. Luque and D. R. Crosley, *computer program by SRI International, SRI report No. MP*, 1999, 99-009.
32. G. C. Chan, J. T. Shelley, J. S. Wiley, C. Engelhard, A. U. Jackson, R. G. Cooks and G. M. Hieftje, *Anal Chem*, 2011, **83**, 3675-3686.
33. A. Kramida, Ralchenko, Yu., Reader, J. and NIST ASD Team (2020). *National Institute of Standards and Technology, Gaithersburg, MD*. DOI: <https://doi.org/10.18434/T4W30F>.
34. E. A. D. Carbone, C.-G. Schregel and U. Czarnetzki, *Plasma Sources Science and Technology*, 2016, **25**.
35. R. W. B. Pearse and A. G. Gaydon, *The Identification of Molecular Spectra*, John Wiley & Sons, New York, 1st. ed edn., 1976.
36. U. N. Pal, A. K. Sharma, J. S. Soni, S. Kr, H. Khatun, M. Kumar, B. L. Meena, M. S. Tyagi, B. J. Lee, M. Iberler, J. Jacoby and K. Frank, *Journal of Physics D: Applied Physics*, 2009, **42**.
37. Z. Hao, S. Ji, H. Liu and Y. Song, *IEEE Transactions on Plasma Science*, 2014, **42**, 824-832.
38. K. Gazeli, P. Svarnas, P. Vafeas, P. K. Papadopoulos, A. Gkelios and F. Clément, *Journal of Applied Physics*, 2013, **114**.
39. B. Brutschy and H. Haberland, *Physical Review A*, 1979, **19**, 2232-2248.
40. R. Deloche, P. Monchicourt, M. Cheret and F. Lambert, *Physical Review A*, 1976, **13**, 1140.

- 1
 - 2
 - 3
 - 4
 - 5
 - 6
 - 7
 - 8
 - 9
 - 10
 - 11
 - 12
 - 13
 - 14
 - 15
 - 16
 - 17
 - 18
 - 19
 - 20
 - 21
 - 22
 - 23
 - 24
 - 25
 - 26
 - 27
 - 28
 - 29
 - 30
 - 31
 - 32
 - 33
 - 34
 - 35
 - 36
 - 37
 - 38
 - 39
 - 40
 - 41
 - 42
 - 43
 - 44
 - 45
 - 46
 - 47
 - 48
 - 49
 - 50
 - 51
 - 52
 - 53
 - 54
 - 55
 - 56
 - 57
 - 58
 - 59
 - 60
41. J. Stevefelt, J. Pouvesle and A. Bouchoule, *The Journal of Chemical Physics*, 1982, **76**, 4006-4015.
42. L. Alves, G. Gousset and C. Ferreira, *Journal of Physics D: Applied Physics*, 1992, **25**, 1713.
43. Y. B. Golubovskii, V. Maiorov, J. Behnke and J. Behnke, *Journal of Physics D: Applied Physics*, 2002, **36**, 39.
44. S. A. Norberg, E. Johnsen and M. J. Kushner, *Journal of Applied Physics*, 2015, **118**, 013301.
45. J. S. Furter and P. C. Hauser, *Analytical Methods*, 2018, **10**, 2701-2711.
46. I. Dzidic, D. I. Carroll, R. N. Stillwell and E. C. Horning, *Analytical Chemistry*, 1976, **48**, 1763-1768.
47. E. Horning, D. Carroll, I. Dzidic, K. Haegele, M. Horning and R. Stillwell, *Journal of chromatographic science*, 1974, **12**, 725-729.
48. H. Kambara, Y. Mitsui and I. Kanomata, *Analytical Chemistry*, 1979, **51**, 1447-1452.
49. A. Qayyum, S. Zeb, M. A. Naveed, S. A. Ghauri, A. Waheed and M. Zakauallah, *Plasma Devices and Operations*, 2006, **14**, 61-70.
50. S. C. Ostrander and J. C. Weisshaar, *Chemical Physics Letters*, 1986, **129**, 220-224.
51. T. Martens, D. Mihailova, J. van Dijk and A. Bogaerts, *Analytical Chemistry*, 2009, **81**, 9096-9108.
52. S. B. Olenici-Craciunescu, A. Michels, C. Meyer, R. Heming, S. Tombrink, W. Vautz and J. Franzke, *Spectrochimica Acta Part B: Atomic Spectroscopy*, 2009, **64**, 1253-1258.
53. S. B. Olenici-Craciunescu, S. Müller, A. Michels, V. Horvatic, C. Vadla and J. Franzke, *Spectrochimica Acta Part B: Atomic Spectroscopy*, 2011, **66**, 268-273.
54. M. Endoh, M. Tsuji and Y. Nishimura, *The Journal of chemical physics*, 1983, **79**, 5368-5375.
55. W. Richardson and D. Setser, *The Journal of Chemical Physics*, 1973, **58**, 1809-1825.
56. P. M. Mul and J. W. McGowan, *Journal of Physics B: Atomic and Molecular Physics*, 1979, **12**, 1591-1601.
57. R. Zaplotnik, M. Bišćan, D. Popović, M. Mozetič and S. Milošević, *Plasma Sources Science and Technology*, 2016, **25**, 035023.
58. B. L. M. Klarenaar, O. Guaitella, R. Engeln and A. Sobota, *Plasma Sources Science and Technology*, 2018, **27**, 085004.
59. W. E. Curtis, *Proceedings of the Royal Society of London. Series A, Containing Papers of a Mathematical and Physical Character*, 1913, **89**, 146-149.
60. P. C. Hill, *Physical Review A*, 1989, **40**, 5006-5016.
61. W. G. Rellergert, S. B. Cahn, A. Garvan, J. C. Hanson, W. H. Lippincott, J. A. Nikkel and D. N. McKinsey, *Phys Rev Lett*, 2008, **100**, 025301.
62. R. J. Van Sonsbeek, R. Cooper and R. N. Bhave, *The Journal of Chemical Physics*, 1992, **97**, 1800-1806.
63. J. B. Gerardo and M. A. Gusinow, *Physical Review A*, 1971, **3**, 255-267.
64. P. L. Patterson, *The Journal of Chemical Physics*, 1968, **48**, 3625-3631.
65. T. Martens, A. Bogaerts, W. J. M. Brok and J. J. A. M. van der Mullen, *Journal of Analytical Atomic Spectrometry*, 2007, **22**.
66. T. Martens, A. Bogaerts, W. Brok and J. van Dijk, *Anal Bioanal Chem*, 2007, **388**, 1583-1594.
67. P. C. Cosby, *The Journal of Chemical Physics*, 1993, **98**, 9560-9569.
68. G. B. Rusu, A. V. Nastuta, A. S. Chiper and G. Popa, 2008.
69. D. Riès, G. Dilecce, E. Robert, P. F. Ambrico, S. Dozias and J. M. Pouvesle, *Journal of Physics D: Applied Physics*, 2014, **47**, 275401.
70. J. Winter, J. S. Sousa, N. Sadeghi, A. Schmidt-Bleker, S. Reuter and V. Puech, *Plasma Sources Science and Technology*, 2015, **24**, 025015.

- 1
- 2
- 3
- 4 71. A. Schmidt-Bleker, S. A. Norberg, J. Winter, E. Johnsen, S. Reuter, K. D. Weltmann and M.
- 5 J. Kushner, *Plasma Sources Science and Technology*, 2015, **24**.
- 6 72. F. Fanelli and F. Fracassi, *Surface and Coatings Technology*, 2017, **322**, 174-201.
- 7 73. K. Nakazawa, S. Yamamoto, E. Nakagawa, A. Ogino, M. Shimomura and F. Iwata, *AIP*
- 8 *Advances*, 2020, **10**, 095103.
- 9 74. K. Fricke, H. Steffen, T. von Woedtke, K. Schröder and K.-D. Weltmann, *Plasma Processes*
- 10 *and Polymers*, 2011, **8**, 51-58.
- 11 75. H. Kuwahata and T. Yamaguchi, *e-Journal of Surface Science and Nanotechnology*, 2016,
- 12 **14**, 231-236.
- 13 76. M. Hofmans, P. Viegas, O. v. Rooij, B. Klarenaar, O. Guaitella, A. Bourdon and A. Sobota,
- 14 *Plasma Sources Science and Technology*, 2020, **29**, 034003.
- 15 77. Y. Zhang, X. Ma, S. Zhang, C. Yang, Z. Ouyang and X. Zhang, *Analyst*, 2009, **134**, 176-181.
- 16 78. J. F. Garcia-Reyes, J. D. Harper, G. A. Salazar, N. A. Charipar, Z. Ouyang and R. G. Cooks,
- 17 *Analytical Chemistry*, 2011, **83**, 1084-1092.
- 18
- 19
- 20
- 21
- 22
- 23
- 24
- 25
- 26
- 27
- 28
- 29
- 30
- 31
- 32
- 33
- 34
- 35
- 36
- 37
- 38
- 39
- 40
- 41
- 42
- 43
- 44
- 45
- 46
- 47
- 48
- 49
- 50
- 51
- 52
- 53
- 54
- 55
- 56
- 57
- 58
- 59
- 60